Geophysical Journal International

Geophys. J. Int. (2023) **234,** 2429–2435
Advance Access publication 2023 June 23
GJI Applied and Marine Geophysics

https://doi.org/10.1093/gji/ggad252

Rock acoustics of CO_2 storage in basalt

José M. Carcione,[1,2] Ayman N. Qadrouh,[3] Mamdoh Alajmi,[3] Naif B. Alqahtani[3] and Jing Ba[1]

[1]*School of Earth Sciences and Engineering, Hohai University, Nanjing 210098, China. E-mail: jba@hhu.edu.cn*
[2]*National Institute of Oceanography and Applied Geophysics GS, Trieste 34010, Italy*
[3]*KACST, PO Box* 6086, *Riyadh* 11442, *Saudi Arabia*

Accepted 2023 June 16. Received 2023 June 16; in original form 2023 April 17

SUMMARY

We simulate variations in the P- and S-wave velocities due to CO_2 injection in basalt, caused by water replacement and mineralization in the form of carbonate cements. Carbonization can be monitored with seismic data on the basis of changes in velocity. We consider basalts composed of (Fe, Ca and Mg) minerals mainly, and the pore space is assumed to be initially saturated with water. The mineralization is based on a model that estimates the volume of precipitated cement and resulting porosity loss, and the velocities as a function of injection time are calculated with a patchy cement model. In the example, there are two stages: 1 week of CO_2 injection and 29 weeks of frame cementation. After 1 week, water has been replaced by CO_2, where density and P-wave velocity decrease, and cementation implies an increase in bulk density, P-wave velocity, whereas porosity and surface area are reduced. To our knowledge there are no models relating the effects of carbon mineralization on seismic properties. The present model can be applied to other rocks, where CO_2 injection induces mineralization and storage.

Key words: Composition and structure of the continental crust; Microstructure; Acoustic properties; Wave propagation.

1 INTRODUCTION

Storage of carbon dioxide (CO_2) in volcanic rocks, such as basalt, peridotite and tuffaceous rocks, rich in reactive and divalent cations, is a valid approach for reducing the amount of greenhouse gases in the atmosphere (e.g. Lackner *et al.* 1995; Takaya *et al.* 2015; Wu *et al.* 2021).

The southwestern coastal region of Saudi Arabia has a dense sequence of Oligocene basalts in the Jizan Group, which have accumulated along the continental rift which preceded the opening of the Red Sea. These basalts are intended for disposal of CO_2 emitted from industrial sources due to carbon mineralization in the subsoil processes. Oelkers *et al.* (2022) reviewed the geology and geochemistry of the basalts of the Jizan Group and evaluated the reactivity of representative samples. Their results assess the fate of dissolved CO_2 in water injected into the Jizan Group. The CO_2-charged water will carbonate when interacting with the basaltic rocks, and would fix more than 95 per cent of injected water-dissolved CO_2 within 5 yrs at 100 °C. Fedorik *et al.* (2023) state that the Jizan Group is one of the principal CO_2 sinks that can help fulfil the decarbonization expectations of the country.

Basalts react with a CO_2–water mixture, resulting in the precipitation of minerals. In particular, Adam *et al.* (2013) reacted three ferro-basaltic samples from the Snake River Plain with a water–CO_2 mixture. They observed that after 30 weeks carbonates precipitated in the pore space, within grain contacts and microcracks reducing the rock permeability and stiffening the rock. CO_2 injection in basalts can increase or decrease the wave velocities. Actually, a small amount (<5 per cent vol.) of carbonate precipitation (Adam *et al.* 2013) or glass dissolution (Kanakiya *et al.* 2017; Saxena *et al.* 2018) results in a change in P-wave velocity of up to 22 and −14 per cent, respectively, for short-term experiments. As for the experimental data, we used those of L. Adam and coworkers, who were the only research group to study this problem. However, in fig. 1 of Otheim *et al.* (2011), only a schematic representation of the process is shown.

The mineralization process is similar to a diagenesis one, where minerals precipitate from solution and cement grain contacts and fill cracks, with a reduction in porosity (Pytte & Reynolds 1989; Walderhaug 1996; Lander & Walderhaug 1999). The acoustics of mineralization and cementation has scarcely been attacked from a theoretical point of view. Khatiwada *et al.* (2012) performed a feasibility study of time-lapse seismic monitoring of CO_2 sequestration in a basalt reservoir. They computed wave propagation simulations, but the combined fluid substitution (CO_2 replaces water) and mineralization effects on the elastic properties are shown schematically (qualitatively).

The mineralization approach starts by a computation of the volume of carbonate cement precipitated in the pore volume by using the Walderhaug (1996) model, which gives the fraction of cement, porosity and surface area of the pore space as a function of the injection time. According to Walderhaug (1996), the first stage is precipitation and then cementation starts to be effective. The process depends on the effective radii of the grains (and surface area), with small grains producing more cement. Roughly, the porosity loss is equal to the volume of precipitated carbonates (Lander & Walderhaug 1999).

A petro-elastical model yields the seismic velocities of the rock. The approach is based on the contact–cement theory (CCT) of Dvorkin & Nur (1996), assuming cement deposited at grain contacts (scheme 1 in Mavko *et al.* 2020, p. 355), and the Hertz–Mindlin (HM) theory (see also Avseth *et al.* 2010, 2016). Then, the Voigt–Reuss–Hill averages and Gassmann equation yield the wet-rock moduli, with the self-consistent (SC) model used to obtain the properties of the mineral mixture (Dvorkin *et al.* 1999).

2 THEORY

2.1 Mineral cement precipitation

Basalts are rich in iron, magnesium and calcium, with a minor percentage of silica (quartz). Basalts react with a CO_2–water mixture, resulting in the precipitation of minerals (Ca, Mg and Fe cations) between adjacent grains and cracks and microfractures, which are assumed to contribute as grain contacts in the proposed acoustic theory given in the next section. To our knowledge, there is no theory to model the effects of cement in fractures on P-wave velocity. The first reaction is the formation of carbonic acid:

$CO_2 + H_2O \rightarrow H_2CO_3$ (carbonic acid)

Then, those cations precipitate as carbonates cements:

(Ca, Mg, Fe) + $H_2CO_3 \rightarrow$ (Ca, Mg, Fe)CO_3 (carbonates) + 2H

Walderhaug (1996) obtained the amount of quartz cement precipitated in a sandstone as a function of time. We use his equations as an *ad hoc* phenomenological approach applied to the precipitation of metal minerals in basalt. The amount of cement (m^3) precipitated in a 1 m^3 of basalt at time t_{l+1} is

$$\phi_p^{l+1} = \phi_0 - (\phi_0 - \phi_p^l)\exp\left[-\frac{aMA_0}{\rho_1\phi_0}\left(10^{bt_{l+1}} - 10^{bt_l}\right)\right], \tag{1}$$

where ϕ_p^l is the amount of mineral cement present at time t_l, ϕ_0 is the initial porosity, a and b are constants, which have units of mol m^{-5} and s^{-1}, respectively, ρ_1 is the grain density, M [kg mol^{-1}] is the molar mass of mineral and is the initial mineral surface area,

$$A_0 = \frac{6FV}{D}, \tag{2}$$

where D is the grain diameter, F is the fraction of mineral in the rock compared to silica and V is a unit volume (1 m^3 if D is given in metres).

In the first time step, $t_0 = 0$, $\phi_p^0 = 0$ and

$$\frac{\phi_p^1}{\phi_0} = 1 - \exp\left[-\frac{aMA_0}{\rho_1\phi_0}(10^{bt_1} - 1)\right], \quad t_1 = \mathrm{d}t, \tag{3}$$

where dt is the time step.

The porosity varies as

$$\phi = \phi_0 - \phi_p \quad \left(\phi^l = \phi_0 - \phi_p^l\right) \tag{4}$$

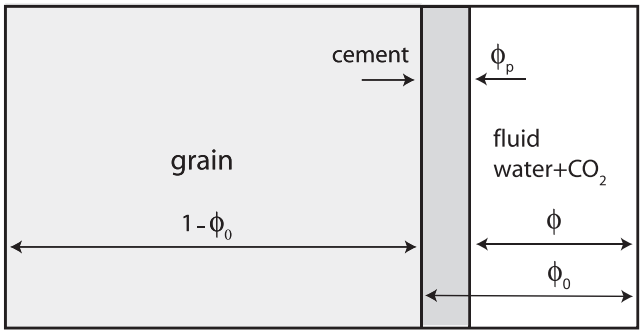

Figure 1. Simplified scheme showing basalt after cementation, where ϕ_p is the cement fraction bonded to the grains. Water is absent after complete CO_2 injection, where cementation initiates.

and the surface area as

$$A = A_0\frac{\phi}{\phi_0}. \tag{5}$$

2.2 Acoustic patchy-cement model

We consider a petro-elastical model to obtain the P- and S-wave velocities as a function of injection time. For the equations regarding the Voigt, Reuss and Hashin–Shtrikman (HS) averages, we refer to Mavko *et al.* (2020). Dvorkin & Nur (1996) developed an elastic model, called contact cement theory (CCT), considering spherical grains (see also Avseth *et al.* 2016; Mavko *et al.* 2020, p. 354). We indicate with the subscripts 1 and 2, the properties of the grains and of the cement, respectively. The model first assumes that the rock is a random pack of grains with porosity close to the critical one ($\phi_c \approx 0.36$, a critical porosity) and an average number of grain contacts $C = 9$. The bulk and shear moduli are

$$K_a = \frac{C}{6}(1-\phi_c)\left(K_2 + \frac{4}{3}\mu_2\right)S_\perp \quad \text{and} \quad \mu_a = \frac{3}{5}\left[K_a + \frac{1}{4}C(1-\phi_c)\mu_2 S_t\right], \tag{6}$$

respectively, where K_2 and μ_2 are the cement bulk and shear moduli, and $S_\perp$ and S_t are related to the normal and shear stiffnesses of a cemented two-grain combination, respectively. The explicit expressions of these stiffnesses are given in Mavko *et al.* (2020, p. 355) and depend on the Poisson ratio of the grains $\nu_1 = (3K_1 - 2\mu_1)/(6K_1 + 2\mu_1)$, where K_1 and μ_1 are the grain bulk and shear moduli, and on

$$\alpha = 2\left[\frac{\phi_p}{3C(1-\phi_c)}\right]^{1/4}, \tag{7}$$

the ratio of the radius of the cement layer to the grain radius, when all cement is deposited at grain contacts. Fig. 1 shows a scheme of the rock after cementation, where ϕ_p is the fraction of cement bonded to the grains, after the water replacement by CO_2 injection.

The rock is an effective medium composed of a binary mixture of cemented grains and loose, unconsolidated ones. Following Avseth *et al.* (2016), the high-porosity limit moduli, K_b and μ_b, are obtained by combining the CCT (K_a–μ_a) and HM (K_u–μ_u) uncemented moduli (see Appendix A) on the basis of the HS upper bound (Appendix B), where the volume fraction of cemented rock to be used in the HS bound is $\beta_1 = \phi_p/\phi_0$, i.e., 0 if there is no cement, and 1 if the whole pore-space is filled with cement.

Then, the SC theory is applied to obtain the moduli K_s and μ_s of a medium where all the pores are filled with cement (see Appendix C). There are two phases, grain and cement (subindices 1 and 2). To this purpose, we use eq. (C1) with $n = 2$, $\phi_1 = (1-\phi_0)/(1-\phi_0 +$

$\phi_p) = (1-\phi_0)/(1-\phi)$, since $\phi = \phi_0 - \phi_p$, $\phi_2 = 1-\phi_1$, $K = K_s$ and $\mu = \mu_s$.

Next, we interpolate between the effective high-porosity member given by the HS upper bound and the mineral phase (i.e. zero porosity) using the Voigt–Reuss–Hill average, that is an arithmetic average of the Voigt and Reuss moduli, to obtain the dry-rock bulk and shear moduli:

$$K_m = \frac{1}{2}(K_V + K_W) \quad \text{and} \quad \mu_m = \frac{1}{2}(\mu_V + \mu_W), \tag{8}$$

where

$$K_V = (1-\phi/\phi_c)K_s + (\phi/\phi_c)K_b, \quad \frac{1}{K_W} = \frac{1-\phi/\phi_c}{K_s} + \frac{\phi/\phi_c}{K_b}, \tag{9}$$

$$\mu_V = (1-\phi/\phi_c)\mu_s + (\phi/\phi_c)\mu_b \quad \text{and} \quad \frac{1}{\mu_W} = \frac{1-\phi/\phi_c}{\mu_s} + \frac{\phi/\phi_c}{\mu_b}. \tag{10}$$

Finally, the wet-rock moduli are obtained with the Gassmann equations (e.g. Mavko *et al.* 2020; Carcione 2022). The bulk and shear moduli are given by

$$K_G = K_m + \alpha^2 M, \quad \mu = \mu_m, \tag{11}$$

where

$$M = \left(\frac{\alpha-\phi}{K_s} + \frac{\phi}{K_f}\right)^{-1}, \tag{12}$$

$$\alpha = 1 - \frac{K_m}{K_s}. \tag{13}$$

and K_f is the fluid modulus.

3 SEISMIC VELOCITIES

The P-wave modulus and velocity are

$$E = K_G + \frac{4}{3}\mu_m. \tag{14}$$

and

$$V_P = \sqrt{\frac{E}{\rho}}, \tag{15}$$

respectively, where ρ is the composite density, given by

$$\rho = (1-\phi)\sum_{i=1}^{2}\beta_i\rho_i + \phi\rho_f, \tag{16}$$

where ρ_i and ρ_f are the densities of the i-th solid phase and fluid, respectively.

Similarly, the S-wave velocity is

$$V_S = \sqrt{\frac{\mu}{\rho}}, \tag{17}$$

In the initial water-replacement period (no cement), the properties of the water–CO_2 mixture are obtained as

$$K_f = \left(\frac{S_w}{K_w} + \frac{S_g}{K_g}\right)^{-1} \tag{18}$$

and

$$\rho_f = S_w\rho_w + (1-S_w)\rho_g, \tag{19}$$

where the subindices 'w' and 'g' refer to water and CO_2, respectively.

At high frequencies the pore-fluid pressures are unrelaxed and ultrasonic moduli have to be considered. Adam & Otheim (2013), for instance, use squirt-flow models.

In summary, a workflow of the modelling process is as follows:

(i) Consider the rock as a random pack of grains with porosity close to the critical one and compute the bulk and shear moduli.
(ii) Obtain the high-porosity limit moduli by combining the previous moduli with the HM uncemented moduli on the basis of the Hashin–Shtrikman upper bound.
(iii) Use a SC theory to obtain the moduli of a medium where all the pores are filled with cement (mineral phase).
(iv) Interpolate between the effective high-porosity member and the mineral phase (i.e., zero porosity) using the Voigt–Reuss–Hill average to obtain the dry-rock moduli.
(v) Finally, the wet-rock moduli are obtained with the Gassmann equations.

4 EXAMPLE

4.1 Mineralization and cementation

Let us consider a ferro-basalt rock as in Adam *et al.* (2013), with an iron oxide (Fe_2O_3) content greater than 16 per cent. The sample has two pore-size distributions at 0.7–8 and 15–100 μm. This difference indicates that there is significant variation in the pore surface area, an important parameter controlling mineralization. A precipitate is developing and after 30 weeks of reactions and carbonate precipitation, porosity decreased from 18.08 per cent to 17.28 per cent. Helium permeability and porosity measurements were performed at a confining pressure of 17.2 MPa. The experiment sets a CO_2-water mixture at 3.5 mol l^{-1} concentration for the 30 weeks. Pressure and temperature in the vessel are 8.3 MPa and 100 °C, respectively, representative of conditions at 1 km depth, where the gas is supercritical, with low viscosity and a density of a liquid.

In the example we consider three elements, namely, $FeCO_3$, $CaCO_3$ and $MgCO_3$, with molar masses of 116, 100 and 84 g mol^{-1}, respectively, and with an average value of $M = 100$ g mol^{-1}, used in eq. (3). On the other hand, the specific surface area in Kanakiya *et al.* (2017) of a basalt with 17.6 per cent porosity is 1610 m^{-1} (see their table 2), and we set the grain diameter $D = 2.6$ mm to honour this value. Moreover, we consider the following properties: $\phi_0 = 18.08$ per cent, $a = 2.22 \times 10^{-3}$ mol m^{-5}, $b = 10^{-7}$ s^{-1}, $\rho_1 = 2.8$ g cm^{-3}, $F = 0.7$ and $V = 1$ m^3. The time step to solve eq. (1) is d$t = 8.41$ h.

Fig. 2 shows the cement fraction and porosity (a) and the surface area (b) as a function of time. As can be seen, the reduction in porosity follows that of the experiments after 30 weeks of reactions and the surface area is reduced, as expected. From eq. (2) we see that the exponent in eq. (1) is proportional to F/D so that the effect of increasing the grain diameter is similar to that of decreasing the detrital content, i.e., the amount of precipitated cement is less in coarse-grain basalts, because of the reduced surface area, compared to fine-grain basalts.

4.2 Wave velocities

4.2.1 Water replacement

At the initial stage, water is being replaced by CO_2. We consider that complete replacement takes place on 1 week and that water

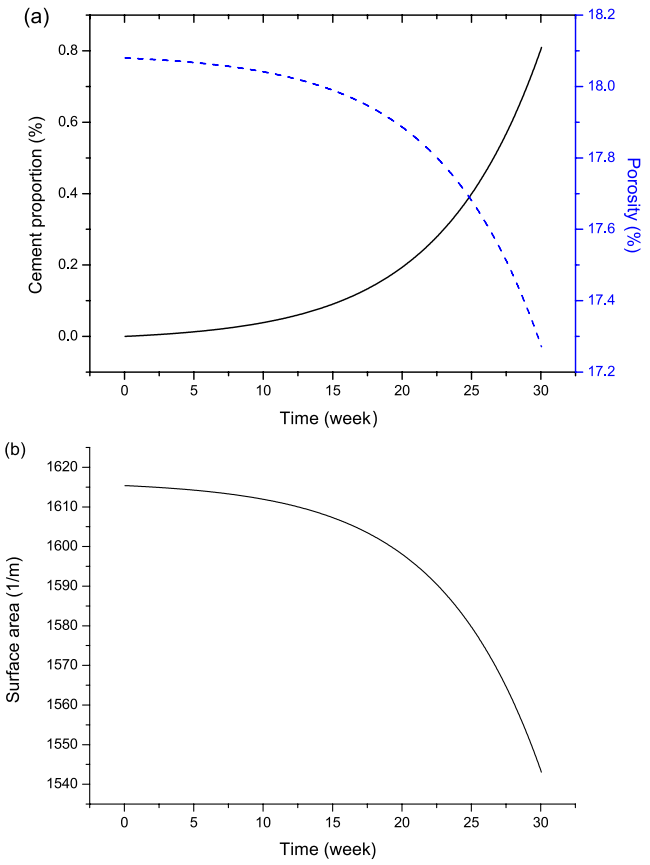

Figure 2. Cement fraction ϕ_p and porosity ϕ (a), and surface area (b), as a function of time.

saturation S_w is proportional to the injection time t as

$$S_w = (1 - t[\text{week}])^2.$$

The grain bulk and shear moduli are $K_1 = 80.1$ GPa (Adam & Otheim 2013) and $\mu_1 = 31$ GPa, and we assume $\rho_1 = 2.8\ \text{g cm}^{-3}$. The conditions are such that the confining and pore pressures are 17.2 and 8.3 MPa, respectively, such that CO_2 is in a supercritial state. At the fluid pressure and temperature of these experiments, the fluid moduli are 0.159 and 2.237 GPa for CO_2 and water, respectively, whereas the respective densities are 832 and 1040 kg m^{-3} (Adam & Otheim 2013).

To estimate the velocities, the fluid-mixture bulk modulus is averaged using the Reuss equation and the fluid density is averaged using an arithmetic mean, as in eqs (18) and (19), respectively.

4.2.2 Cementation

During the 30 weeks of injection, elastic waveforms are recorded at 0.5 MHz on dry samples to analyse the changes to the rock frame after basalt and CO_2 have reacted. The samples are taken out of the vessel after 15 weeks and oven dried at 50 °C before recording ultrasonic waveforms again. These steps are then repeated for another 15 weeks (Adam *et al.* 2013). Since the dry-rock velocities are frequency independent, their values can be used at seismic frequencies.

The elastic properties (bulk modulus, shear modulus and density) of the cements are taken from https://materialsproject.org/materials/mp-18969/ to be: $CaCO_3 = 76$, 32 and 2610; $FeCO_3 = 111$, 23 and 3780; $MgCO_3 = 105$, 63 and 2900 (in GPa, GPa and kg m^{-3}, respectively). Assuming equal composition, and using the Voigt–Reuss–Hill average for the moduli and the arithmetic mean for the density, we obtain the effective elastic properties of the cement, i.e., $K_2 = 96$ GPa, $\mu_2 = 36$ GPa and $\rho_2 = 3097\ \text{kg m}^{-3}$. The density and bulk modulus of CO_2 are $832\ \text{kg m}^{-3}$ and 0.159 GPa, respectively (Adam & Otheim 2013). Moreover, $\delta = 0.01$ MPa and $p_e = 0$ in the HM model.

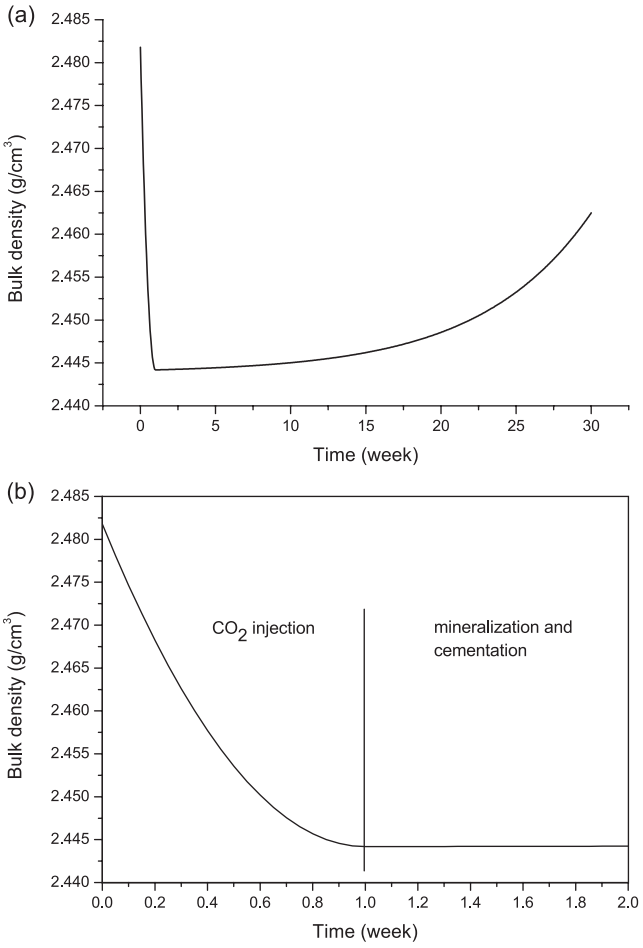

Figure 3. Bulk density as a function of time (a). Panel (b) shows the density in the first 2 weeks.

Fig. 3(a) displays the bulk density as a function of time. Fig. 3(b) clearly shows the two stages, i.e., water replacement during CO_2 injection, where the density decreases and mineralization and cementation after week 1, where the density starts to increase due to the addition of minerals in the grain contacts (see Fig. 1).

The velocities as a function of time are displayed in Fig. 4. The wet-rock velocity is higher that the dry one for high water saturation, but the opposite trend occurs when water is replaced by CO_2. The S-wave wet-rock velocity is always lower than the dry one, because the bulk density increases and the shear modulus does not depend on the properties of the fluids. Panel (b) shows the wet-rock P-wave velocity corresponding to the two stages: CO_2 injection, where the saturation of water is zero at 1 week; and mineralization and cementation, where the velocity increases due to grain cementation. Fig. 4(b) explains the behaviour of the velocity shown in the schematic diagram of fig. 4 in Khatiwada *et al.* (2012).

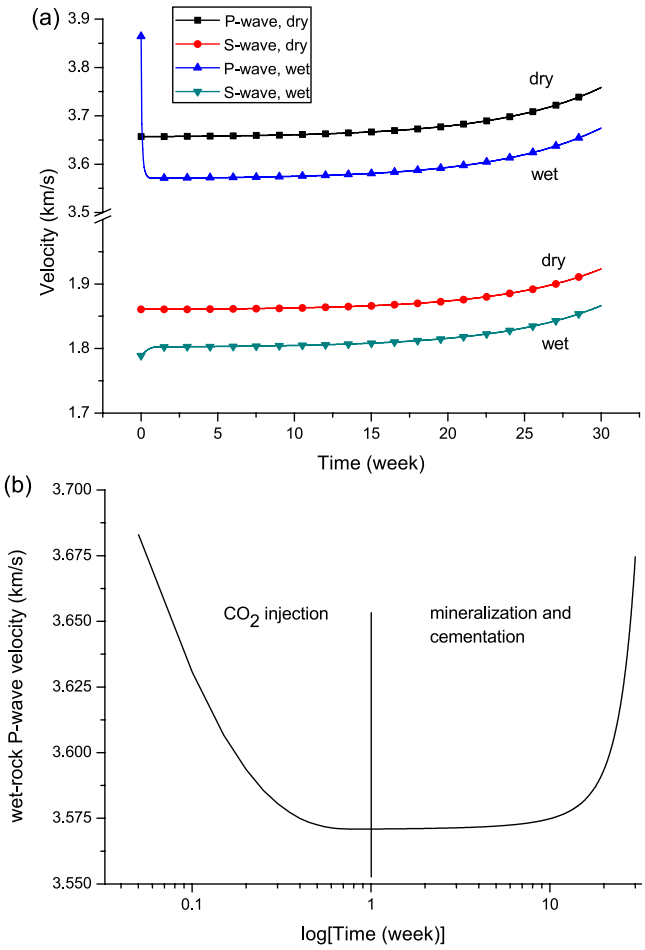

Figure 4. Dry- and wet-rock velocities as a function of time. Panel (b) shows the wet-rock P-wave velocity corresponding to the two stages: CO_2 injection, where the saturation of water is zero at 1 week; and mineralization and cementation, where the velocity increases due to grain cementation.

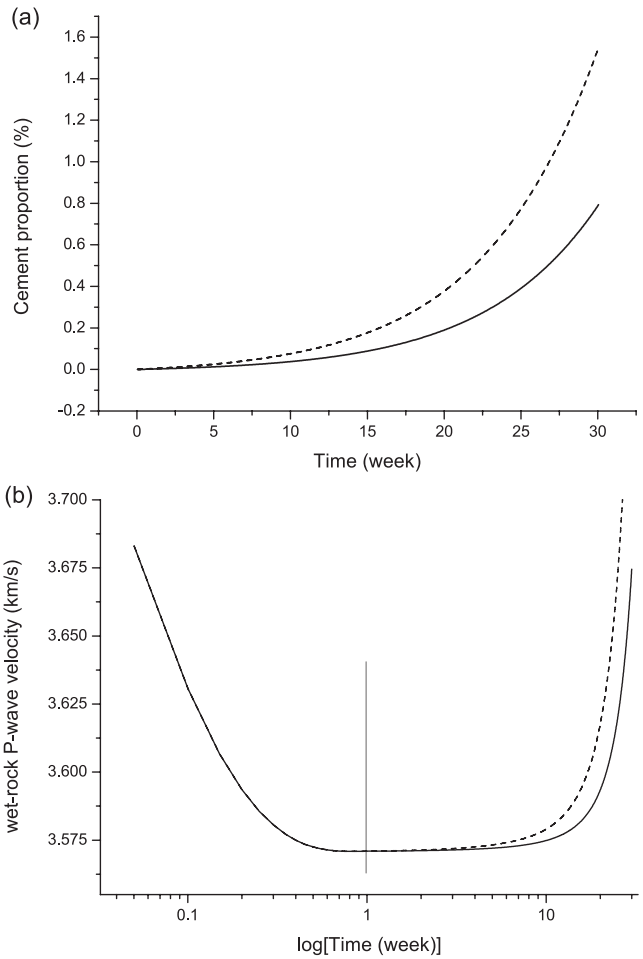

Figure 5. Effect of the grain diameter D on the cement proportion (a) and P-wave velocity (b). The solid and dashed lines correspond to $D = 2.6$ and 1.3 mm, respectively.

Varying the cement stiffness one order of magnitude results in only 15 per cent increase in velocities, an effect much smaller than that of increasing cement content [fig. 11 in Dvorkin *et al.* (1994)].

The effect of the grain diameter D on the cement proportion and P-wave velocity is shown in Fig. 5, where the solid and dashed lines correspond to $D = 2.6$ and 1.3 mm, respectively. In the second case, the surface area is twice that of the first case, and at 30 weeks more cement has been generated and the velocity has slightly increased. In week 10, the velocity difference is only a few metres per second, but as the reaction time increases, the difference increases (in week 30, the difference is about 40 m s^{-1}), indicating that it can be resolved by seismic tomography, for example.

In the case presented here, the reaction time is short, but in geological time the variations in P-wave velocity and bulk density will be more pronounced, that is these quantities increase with carbonation whereas porosity decreases, to the extent that these variations can be resolved by seismic methods. The present model can also be applied to other reactive rocks, such as mafic or ultramafic lithologies, like diabase, gabbro and norite (Snaebjörnsdóttir *et al.* 2020).

The CCT model can be further improved by considering the effects of the contact thickness, i.e., is the minimal distance between two adjacent grains, on the normal and tangential stiffness (Guo & Han 2016), and pre-compaction (Guo & Chen 2022). These effects will be investigated in a future work.

5 CONCLUSIONS

We have developed a quantitative model to simulate the changes in the *P*- and S-wave velocities due to CO_2 injection in basalt, caused by water replacement and mineralization in the form of carbonate cements. The pore space is assumed to be initially saturated with water. The mineralization is based on a model that estimates the volume of precipitated cement and resulting porosity loss, and the velocities as a function of injection time are calculated with a patchy cement model.

In the specific example, the wet-rock velocity is higher that the dry one for high water saturation, but the opposite trend occurs when water is replaced by CO_2. The S-wave wet-rock velocity is always lower than the dry one, because the bulk density increases and the shear modulus does not depend on the properties of the fluids. The wet-rock P-wave velocity has two opposite trends at the two stages: (i) CO_2 injection, where the saturation of water is zero at week 1; bulk modulus and density decrease as well as velocity and (ii) mineralization and cementation, where the rock is fully saturated with supercritical CO_2; density and velocity increases due to grain cementation.

DATA AVAILABILITY

No new data were generated or analysed in support of this research. The code underlying this article will be shared on reasonable request to the corresponding author.

REFERENCES

Adam, L. & Otheim, T., 2013. Elastic laboratory measurements and modeling of saturated basalts, *J. geophys. Res.,* **118,** 840–851.

Adam, L., Wijk, K., Otheim, T. & Batzle, M., 2013. Changes in elastic wave velocity and rock microstructure due to basalt-CO_2-water reactions, *J. geophys. Res.,* **118,** 4039–4047.

Avseth, P., Mukerji, T., Mavko, G. & Dvorkin, J., 2010. Rock-physics diagnostics of depositional texture, diagenetic alterations, and reservoir heterogeneity in high-porosity siliciclastic sediments and rocks – a review of selected models and suggested work flows, *Geophysics,* **75,** 75A31–75A47.

Avseth, P., Skjei, N. & Mavko, G., 2016. Rock-physics modeling of stress sensitivity and 4D time shifts in patchy cemented sandstones – application to the Visund Field, North Sea, *Leading Edge,* **35**(10), 868–878.

Berryman, J.G., 1980. Long-wavelength propagation in composite elastic media II. Ellipsoidal inclusions, *J. acoust. Soc. Am.,* **68,** 1820–1831.

Carcione, J. M., 2022. *Wave Fields in Real Media. Theory and Numerical Simulation of Wave Propagation in Anisotropic, Anelastic, Porous and Electromagnetic Media,* 4th edn, revised and extended, Elsevier Science.

Carcione, J.M., Landrø, M., Gangi, A.F. & Cavallini, F., 2007. Determining the dilation factor in 4D monitoring of compacting reservoirs by rock-physics models, *Geophys. Prospect.,* **55,** 793–804.

Dvorkin, J., Berryman, J., Nur & A, 1999. Elastic moduli of cemented sphere packs, *Mech. Mater.,* **31,** 461–469.

Dvorkin, J., Nur, A. & Yin, H., 1994. Effective properties of cemented granular material, *Mech. Mater.,* **18,** 351–366.

Dvorkin, J. & Nur, A., 1996. Elasticity of high-porosity sandstones: theory for two North Sea data sets, *Geophysics,* **61,** 1363–1370.

Fedorik, J. *et al.*, 2023. Structure and fracture characterization of the Jizan group: implications for subsurface CO_2 basalt mineralization, *Front. Earth Sci.,* **10,** doi:10.3389/feart.2022.946532.

Gangi, A.F. & Carlson, R.L., 1996. An asperity-deformation model for effective pressure, *Tectonophysics,* **256,** 241–251.

Goffe, W.L., Ferrier, G.D. & Rogers, J., 1994. Global optimization of statistical functions with simulated annealing, *J. Econometr.,* **60**(1–2), 65–99.

Guo, J. & Chen, X., 2022. Pressure dependence of elastic wave velocities of unconsolidated cemented sands, *Geophysics,* **87,** MR161–MR175.

Guo, J. & Han, X., 2016. Rock physics modelling of acoustic velocities for heavy oil sand, *J. Petrol. Sci. Eng.,* **145,** 436–443.

Gurevich, B. & Carcione, J.M., 2000. Gassmann modeling of acoustic properties of sand/clay mixtures, *Pure appl. Geophys.,* **157,** 811–827.

Hashin, Z. & Shtrikman, S., 1963. A variational approach to the theory of the elastic behaviour of multiphase materials, *J. Mech. Phys. Solids,* **11,** 127–140.

Hertz, H., 1895. *Gesammelte Werke, Band I,* Schriften Vermischten Inhalts, Leipzig.

Kanakiya, S., Adam, L., Esteban, L., Rowe, M. C. & Shane, P., 2017. Dissolution and secondary mineral precipitation in basalts due to reactions with carbonic acid, *J. geophys. Res.,* **122**(2017), 4312–4327.

Khatiwada, M., Adam, L., Morrison, M. & van Wijk, K., 2012. A feasibility study of time-lapse seismic monitoring of CO_2 sequestration in a layered basalt reservoir, *J. Appl. Geophys.,* **82,** 145–152.

Lackner, K.S., Wendt, C.H., Butt, D.P., Joyce, E.L. & Sharp, D.H., 1995. Carbon dioxide disposal in carbonate minerals, *Energy,* **20,** 1153–1170.

Lander, R.H. & Walderhaug, O., 1999. Predicting porosity through simulating sandstone compaction and quartz cementation, *AAPG Bull.,* **83,** 433–449.

Mavko, G., Mukerji, T. & Dvorkin, J., 2020. *The Rock Physics Handbook: Tools for Seismic Analysis in Porous Media,* Cambridge Univ. Press.

Mindlin, R.D., 1949. Compliance of elastic bodies in contact, *J. Appl. Mech.,* **16,** 259–268.

Oelkers, E. *et al.*, 2022. The subsurface carbonation potential of basaltic rocks from the Jizan region of Southwest Saudi Arabia, *Int. J. Greenhouse Gas Contl.,* **120,** doi:10.1016/j.ijggc.2022.103772.

Otheim, T.L., Adam, L., Van Wijk, K., Batzle, M.L. & Podgorney, R., 2011. CO2 sequestration in basalt: carbonate mineralization and fluid substitution, *Leading Edge,* 1354–1359.

Pytte, A.M. & Reynolds, R.C., 1989. The thermal transformation of smectite to illite, in *Thermal History of Sedimentary Basins: Methods and Case Histories,* pp. 133–140, eds Naeser, N.D. & McCulloh, T.H., Springer–Verlag.

Saxena, V., Krief, M. & Adam, L., 2018. *Handbook of Borehole Acoustics and Rock Physics for Reservoir Characterization,* Elsevier.

Snaebjörnsdóttir, S.O., *et al.*, 2020. Carbon dioxide storage through mineral carbonation, *Nat. Rev. Earth Environ.,* **1,** 90–102.

Takaya, Y., Nakamura, K. & Kato, Y., 2015. Dissolution of altered tuffaceous rocks under conditions relevant for CO_2 storage, *Appl. Geochem.,* **58,** 78–87.

Walderhaug, O., 1996. Kinetic modelling of quartz cementation and porosity loss in deeply buried sandstone reservoirs, *AAPG Bull.,* **80,** 731–745.

Walton, K., 1987. The effective elastic moduli of a random packing of spheres, *J. Mech. Phys. Solids,* **35,** 213–226.

Wu, H., Jayne, R.S., Bodnar, R.J. & Pollyea, R.M., 2021. Simulation of CO_2 mineral trapping and permeability alteration in fractured basalt: Implications for geologic carbon sequestration in mafic reservoirs, *Int. J. Greenhouse Gas Contl.,* **109,** doi:10.1016/j.ijggc.2021.103383.

APPENDIX A: THE HERTZ–MINDLIN MODEL

The Hertz–Mindlin (HM) contact theory, considers a random packing of spheres as an effective medium (Hertz 1895; Mindlin 1949; Walton 1987; Mavko *et al.* 2020). We modify the HM model by replacing the effective pressure p_e, by the augmented value, $p_e + \delta$, following Gangi & Carlson (1996), assuming that the grains are subjected to an initial level of bonding determined by δ (a pre-stress condition). A HM model with augmented effective pressure is given in Carcione *et al.* (2007) to model bonded grains at $p_e = 0$.

Then, the bulk and shear (uncemented) moduli at the critical porosity ϕ_c are given by

$$K_u = \left[\frac{C^2(1-\phi_c)^2\mu_1^2(p_e+\delta)}{18\pi^2(1-\nu_1)^2}\right]^{1/3} \tag{A1}$$

and

$$\mu_u = \frac{3(5-4\nu_1)}{5(2-\nu_1)}K_u, \tag{A2}$$

where μ_1 is the shear modulus of the grains, ν_1 is the Poisson ratio of the grains and C is the average number of contacts per spherical grain.

APPENDIX B: HASHIN AND SHTRIKMAN BOUNDS AND AVERAGES

Let us denote the solid bulk and shear moduli by K_i and μ_i, respectively. A two-solid composite, with no restriction on the shape of the two phases, has stiffness bounds given by the Hashin & Shtrikman (1963) equations,

$$K_{\rm HS}^{\pm} = K_1 + \frac{\beta_2}{(K_2-K_1)^{-1} + \beta_1\left(K_1 + \frac{4}{3}\mu_\beta\right)^{-1}} \tag{B1}$$

and

$$\mu_{\rm HS}^{\pm} = \mu_1 + \frac{\beta_2}{(\mu_2-\mu_1)^{-1} + \beta_1\left[\mu_1 + \frac{\mu_\beta}{6}\left(\frac{9K_\beta+8\mu_\beta}{K_\beta+2\mu_\beta}\right)\right]^{-1}}, \tag{B2}$$

where β_1 and β_2 are the fractions of solid 1 and 2 ($\beta_1 + \beta_2 = 1$), and $\beta_1 = \phi_1/(1-\phi)$. We obtain the upper bounds when K_β and μ_β are the maximum bulk and shear moduli of the single components, and the lower bounds when these quantities are the corresponding minimum moduli, that is we have the upper bound if 1 is the stiffer medium and the lower bound is obtained if 1 is the softer medium (Mavko *et al.* 2020).

The arithmetic averages of the bounds are frequently used to obtain the bulk and shear moduli of a mineral mixture, i.e.,

$$K_s = \frac{1}{2}(K_{\rm HS}^{+} + K_{\rm HS}^{-}), \quad \mu_s = \frac{1}{2}(\mu_{\rm HS}^{+} + \mu_{\rm HS}^{-}). \tag{B3}$$

APPENDIX C: SELF-CONSISTENT (SC) SCHEME

In the SC approximation, the elastic moduli of an unknown effective medium have to be found implicitly. The model has been used by Gurevich & Carcione (2000) to obtain the stiffnesses of sand–clay mixtures, where the inclusions are spherical. Here, we consider spherical grains (aspect ratio $\gamma = 1$) and pores of aspect ratio $\gamma < 1$. In this case, it is $N = 3$ for grain, cement and water.

The effective bulk and shear moduli of the composite medium (K and μ), with N phases and proportion ϕ_i, are obtained as the roots of the following system of equations

$$\begin{aligned} &\textstyle\sum_{i=1}^{N} \phi_i(K_i - K)P_i = 0, \\ &\textstyle\sum_{i=1}^{N} \phi_i(\mu_i - \mu)Q_i = 0, \end{aligned} \tag{C1}$$

where

$$\begin{aligned} P_i &= \frac{K + \frac{4}{3}\mu}{K_i + \frac{4}{3}\mu}, \quad i = 1, \ldots, n \\ Q_i &= \frac{\mu + \zeta}{\mu_i + \zeta}, \\ \zeta &= \frac{\mu}{6}\cdot\frac{9K + 8\mu}{K + 2\mu} \end{aligned} \tag{C2}$$

for the grains, i.e., i =1, 2 (Mavko *et al.* 2020) and $P_3 = \frac{1}{3}T_{iijj}$ and $Q_3 = \frac{1}{5}(T_{ijij} - P)$ (for the pores), where T_{iijj} and T_{ijij} are given in appendix A of Berryman (1980) or in p. 246 of Mavko *et al.* (2020). If $\gamma = 1$, P_3 and Q_3 are given by eq. (C2). A limitation of this theory is that the inclusions are isolated, so that pore pressures are not equilibrated and the model computes high-frequency velocities.

To solve eq. (C1), we use the algorithm developed by Goffe *et al.* (1994). The Fortran code can be found in: https://econwpa.ub.uni-muenchen.de/econ-wp/prog/papers/9406/9406001.txt.